RESEARCH

Facile synthesis of honeycomb-structured biochar with high specific surface and its electrochemical properties as anodes for Na-ion batteries

Wei Zhang[1] · Mingqi Li[1,2] · Yiwen Chen[1] · Zhanwei Zhang[1]

Abstract

High-performance and low-cost electrode material is crucial for the development of Na-ion batteries. Herein, a novel honeycomb-structured biochar with high specific area (labelled as HS X-C) was constructed through a simple and scalable method, using Xanthium sibiricum fruits as starting material with the assistance of NaCl template. The HS X-C shows a long-range-disordered but short-range-ordered microstructure. As an anode for Na-ion batteries, it exhibits an initial coulombic efficiency of about 86.5%, a rate capability of 161 mAh g^{-1} at 4.0 A g^{-1} and a cyclability of 3000 cycles at 2.0 A g^{-1}. Moreover, the Na-ion full cell matched with the NVP/rGO cathode exhibits an average operating voltage of about 3.3 V and a high energy density of about 180 Wh kg^{-1}$_{(total)}$. Kinetic studies indicate that the reaction rate of this anode is jointly controlled by diffusion and pseudocapacitance. This work not only greatly improves the sodium storage performance of the biochar from Xanthium sibiricum fruits, but also demonstrates the importance of the adopted synthesis techniques for the electrochemical performance of biochar.

Keywords Na-ion batteries · Biochar · Honeycomb structure · Anode · Electrochemical performance

Introduction

As an important energy storage device, Li-ion batteries have been widely used in various mobile devices and smart grids because of high energy density, long cycle life and environmental friendliness. However, the limited and unevenly distributed lithium resources seriously influence their sustainable development. Due to similar energy storage mechanism to lithium-ion batteries and abundant sodium resources, Na-ion batteries are expected to replace Li-ion batteries in some areas without strict requirements for volume energy density [1, 2]. Currently, developing high-performance and low-cost electrode materials is the key to the commercialization of Na-ion batteries. According to the sodium storage mechanism, the anode materials studied can

be roughly divided into insertion type [3], conversion type [4–8] and alloy type [9, 10]. Despite of high specific capacity, conversion-type and alloy-type materials suffer from large volume variation during cycling, seriously hindering their practical applications [11]. Hard carbon is considered the most promising anode material for Na-ion batteries due to its easy availability and relatively small volume expansion [12, 13]. However, the challenges of using hard carbon as anodes for Na-ion batteries are its low reversible capacity, high working potentials and low initial coulombic efficiency, which seriously sacrifices the energy density of full batteries [14]. In the available reports, most of hard carbon anodes showed a reversible capacity of less than 200 mAh g^{-1} [15]. Although some heteroatom-doped hard carbon demonstrated relatively high reversible capacity, a considerable portion of the capacity occurred at potentials above 1.5 V as well as without obvious operating potential plateaus [16], and the first coulombic efficiency was below 75%. In addition, complex preparation processes for some hard carbon with special morphology and microstructure greatly increased the cost of materials. In the future, it is very important to find hard carbon anode with high specific capacity, low operating

✉ Mingqi Li
lmingq888@aliyun.com

1 College of Chemistry and Chemical Engineering, China West Normal University, Nanchong 637009, China

2 Chemical Synthesis and Pollution Control Key Laboratory of Sichuan Province, Nanchong 637009, China

potential, high first coulombic efficiency and low cost for the commercialization of sodium-ion batteries.

The use of biomass as raw material to prepare hard carbon has some unique advantages, such as diversity, low cost, low pollution and sustainability [17]. To date, some biochar has been developed to act as anodes for Na-ion batteries [18–24]. For instance, N-doped porous carbon with tailored surface area and pore structure was synthesized by using seaweed as carbon source, delivering a sodium storage capacity of 192 mAh g^{-1} after 500 cycles at 0.2 A g^{-1} [23]. Biomass carbon from the palmyra palm tree maintained 155 mAh g^{-1} sodium storage capacity after 100 cycles at 0.1 A g^{-1} [24]. Uniform hard carbon microtubes (HCTs) were made from natural cotton through the one simple carbonization process [25]. As an anode for Na-ion batteries, the HCTs carbonized at 1300 °C delivered the highest reversible capacity of 315 mAh g^{-1} and good rate capability. Although some progress has been made, significant improvements in key indicators required for practical applications are still needed, such as specific capacity, operating potential, rate capability, cycle life and first coulombic efficiency.

Herein, a novel three-dimensional honeycomb-structured biochar (labelled as HS X-C) was reported. which was synthesized by milling and pyrolysis with the assistance of NaCl hard template, using Xanthium sibiricum fruits as raw material. Xanthium sibiricum usually grows in plains, hills and low mountains. Although it does not require manual management, the fruit yield is high. However, its economic value has not been well exploited. Wang [26] prepared hard carbon by direct pyrolysis of Xanthium sibiricum fruits and investigated the influence of pyrolysis temperature on its electrochemical performance. At 0.05 A g^{-1}, the optimized hard carbon showed a reversible capacity of 252.88 mAh g^{-1} with an initial coulombic efficiency of 69.08%. At 1 A g^{-1}, the discharge capacity kept at 106.23 mAh g^{-1} after 500 cycles. In order to further improve the sodium storage performance of hard carbon from Xanthium sibiricum fruits, we conducted a series of studies to adjust its morphology and microstructure. It was found that the introduction of NaCl hard templates in the material preparation process easily changed the morphology and microstructure of the synthesized hard carbon, thereby significantly enhancing its electrochemical performance as anodes for Na-ion batteries. The final product showed a three-dimensional honeycomb-like structure (labelled as HS X-C). It exhibited a high initial coulombic efficiency of about 86%, an excellent rate capability of 161 mAh g^{-1} at 4.0 A g^{-1} and a long-term cyclability of 3000 cycles at 2.0 A g^{-1}. The assembled Na-ion full cells showed a high average operating voltage of about 3.3 V and a high energy density of about 180 Wh kg^{-1}. In terms with specific capacity, rate capability and cycle life, the HS X-C anodes outperformed most of the previously reported biochar materials (Tab. S1). In addition, the kinetics of the HS X-C anodes in Na-ion batteries was also systematically investigated.

Experimental section

Material synthesis

Scheme S1 shows the synthesis schematic diagram of the HS X-C. Xanthium sibiricum fruits were taken from nature. After washing and drying, they were ground into powder with a grinder. Then, 2 g powder and 8 g NaCl were added into a steel tank with a ball-to-material ratio of 15:1 and milled on a planetary mill at 550 rpm for 6 h; subsequently, the high-temperature treatment was divided into two stages. First, the milled mixture was transferred to a corundum boat and annealed at 600 °C for 2 h in an argon atmosphere. After natural cooling, the solid was washed with distilled water to remove NaCl. Second, the collected product was dried at 110 °C in vacuum for 8 h and then further annealed in argon at 1000 °C for 2 h. The final product was labelled as HS X-C. For comparison, the hard carbon from Xanthium sibiricum fruits without the assistance of NaCl template was prepared through directly annealing the milled Xanthium sibiricum fruits at 1000 °C for 2 h, which was labelled as X-C. During annealing treatments, heating rate and argon flow used were 5 °C min^{-1} and 80 mL min^{-1}, respectively.

Material characterization

The morphology, microstructure and composition of the synthesized products were characterized using scanning electron microscopy (SEM, Gemini-500), transmission electron microscopy (TEM, JEOL 2100F) and energy dispersive spectroscopy (EDS, Oxford max150). The specific surface area measurement was performed on a Micromeritics 2460 tester at 77 K, during which N_2 was used as the adsorption/desorption gas. The graphitization degree of carbon was investigated by an X-ray diffractometer (XRD, D8 Discover) and a Raman spectrometer (Witec alpha300). The chemical states and contents of the elements were detected by X-ray photoelectron spectroscopy (Escalab 250xi) and elemental analysis (EA, elementar vario EL cube).

Electrochemical measurement

The Na$^+$ storage properties of the as-synthesized hard carbon were measured by the assembled 2032 cells. The working electrode was composed of the tested material, Super P carbon black and sodium alginate in a weight ratio of 75:10:15, in which copper foil served as the current collector and the active material loading was about 1.0 mg cm^{-2}. In a half cell, the counter electrode was Na metal disc. In a

full cell, the cathode was composed of $Na_3V_2(PO_4)_3$/rGO, the preparation of which was referred to our previous work [27], Super P carbon black and polyvinylidene fluoride in a weight of 83:10:7. The positive and negative capacity ratio is 1:1.2. The electrolyte was 1 M $NaPF_6$ in diglyme, while the separator was glass fibre (Whatman GF/A). Galvanostatic charge/discharge and galvanostatic intermittent titration (GITT) measurements were performed on a Neware battery tester. Cyclic voltammetry (CV) and electrochemical impedance spectrum (EIS) measurements were performed on an EC-lab electrochemical workstation. The amplitude and frequency range for EIS were 10 mV and 100 kHz–100 mHz, respectively.

Results and discussion

The SEM images of the X-C synthesized from directly pyrolyzing ground Xanthium sibiricum fruits are shown in Fig. S1. It was irregular solid blocks with obvious agglomeration characteristics. However, with the introduction of NaCl hard template, the synthesized HS X-C showed significant difference in morphology and microstructure.

From Fig. 1a and b, it delivered a three-dimensional honeycomb-like structure with a wall thickness of less than 20 nm. The TEM image in Fig. 1c further confirmed this kind of special structure. HRTEM image revealed that the HS X-C was long-range-disordered but short-range-ordered in terms of crystalline property (Fig. 1d). The (002) lattice spacing was around 0.37 nm, which was larger than 0.335 nm for the graphite [28]. The discontinuous lattice strips should be attributed to the abundance of heteroatoms in biomass raw materials. During the heat treatment, some non-metallic heteroatoms could be doped into C, while the others were released in gas form. In addition, the etching of metal ions could also lead to discontinuity of lattice strips. Elemental analysis showed that the N and O heteroatom contents were about 1.1% and 5.2%, respectively, but no S element was detected. From the hierarchical elemental distribution map in Fig. S2, the doped N and O elements were distributed

Fig. 1 **a**, **b** SEM images, **c** TEM and (**d**) HRTEM images, **e** N_2 adsorption/desorption isotherms and (**f**) pore size distribution curve of the HS X-C
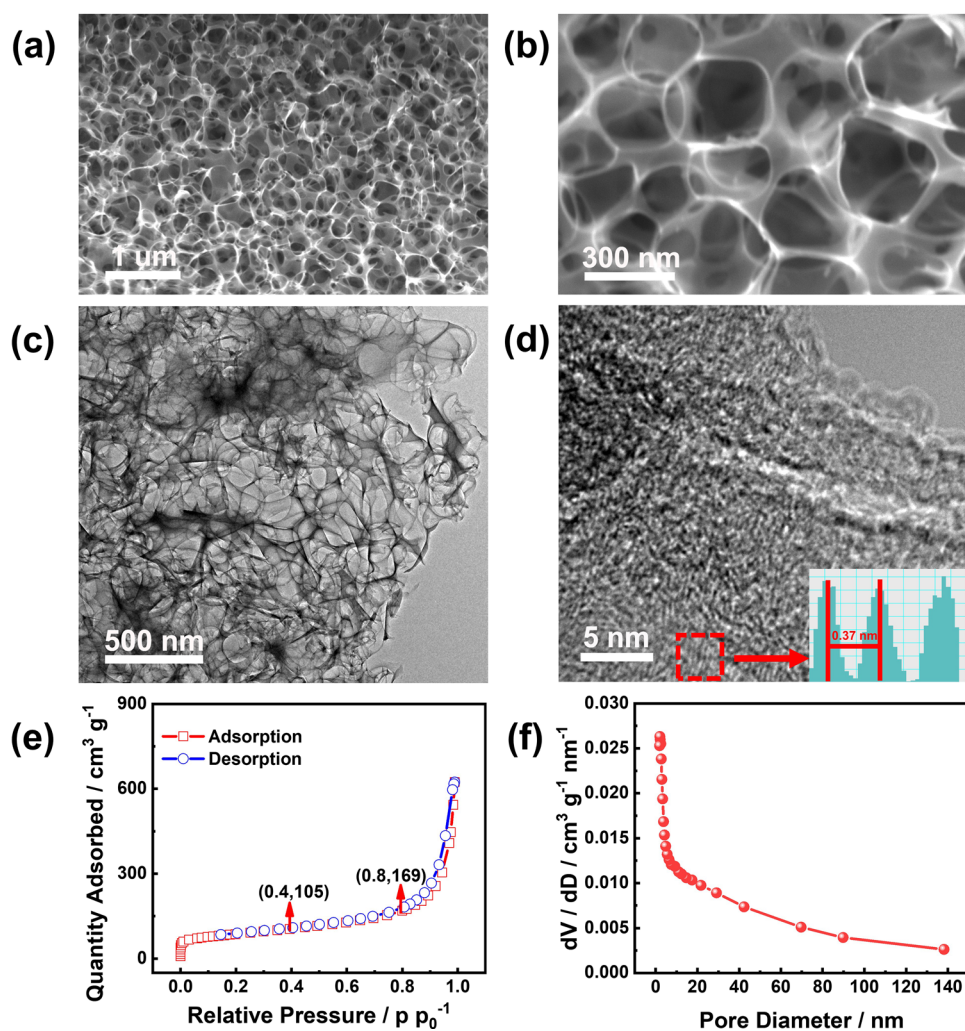
evenly. Figure 1e shows the N_2 adsorption–desorption isotherms of the HS X-C. When the relative pressure (p/p_0) increased from 0 to 0.4, the amount of adsorbed N_2 reached 105 cm^3 g^{-1}, indicating that there were many micropores. During the increase of p/p_0 from 0.4 to 0.8, the amount of adsorbed N_2 increased only by 64 cm^3 g^{-1}. Considering that no obvious hysteresis ring appeared between 0.4 and 0.8, the number of middle pores was relatively small. After p/p_0 exceeded 0.8, the amount of adsorbed N_2 increased rapidly with increasing pressure, indicative of the existence of many macropores [29]. These characteristics were well accorded with the pore size distribution curve in Fig. 1f. Calculated on the desorption isothermal curve, the BET surface area and total pore volume of the HS X-C were about 299 m^2 g^{-1} and 0.91 cm^3 g^{-1}, respectively. The high specific surface area and abundant voids contributed to improving the contact area between material and electrolyte, facilitating the penetration of electrolyte, promoting the transportation of ions and easing the relaxation of the tension, so the HS X-C was expected to exhibit high capacity and excellent rate performance.

The XRD pattern and Raman spectrum of the HS X-C are shown in Fig. 2a and b. Although no sharp peak was observed in the XRD pattern, two obvious broad peaks appeared at 23° and 43°, which were assigned to (002) and (100) planes of graphite respectively. Such a situation was consistent with a short-range-ordered structure. In the Raman spectrum, two peaks were assigned to the vibration of disordered carbon (D-band) and graphitized carbon

(G-band) were located at 1350 and 1580 cm^{-1}, respectively. The fitting analysis revealed that the peak intensity ratio (I_D/I_G) was about 0.85, further confirming that the HS X-C had a relatively high graphitization. XPS was used to detect the chemical composition of the surface. As shown in Fig. 2c, the chemical composition was relatively simple, where only C, N and O elements were detected. The C 1s HRXPS spectrum could be fitted into four peaks at 284.4, 285, 285.9 and 287.4 eV, corresponding to C–C, C-N, C-O and C=O bonds, respectively (Fig. 2d) [30]. The N 1s HRXPS spectrum could be deconvoluted into two peaks at 398 and 400 eV (Fig. 2e), which belonged to pyridinic N and pyrrole N, respectively [23]. The O 1s HRXPS spectrum could be divided into three peaks at 531.1, 532.2 and 533.2 eV, which corresponded to C=O, C-O and C–O–C bonds, respectively (Fig. 2f) [31]. These results showed that both N and O were doped into C host. Compared with C atom, since N and O had redundant free electrons and higher electronegativity, it was easy to cause electric field imbalance, thereby providing more adsorption sites for alkali metal ions [32].

The electrochemical behaviour of the HS X-C as an anode of Na-ion batteries was investigated. Figure 3a shows its initial three CV curves at 0.2 mV s^{-1}. A pair of sharp redox peaks presented at approximately 0.044 and 0.095 V with a peak potential difference of 51 mV. The other peaks were very weak and broad. In addition, it was interesting that even in the first cathodic scan, no distinct peak of electrolyte decomposition was observed, implying that the anode could possess a high first coulombic efficiency. Figure 3b
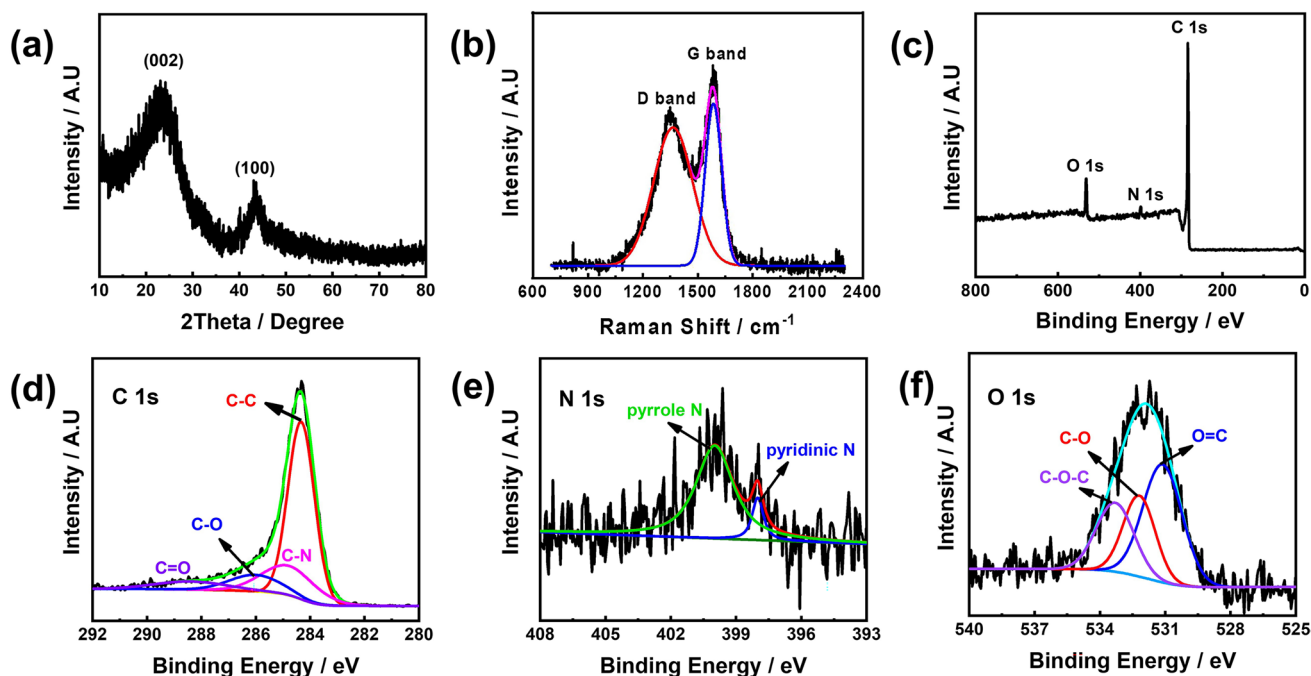

Fig. 2 **a** XRD pattern, **b** Raman spectrum, **c** XPS survey, **d** C 1s HRXPS, **e** N 1s HRXPS and (**f**) O 1s HRXPS spectra of the HS X-C
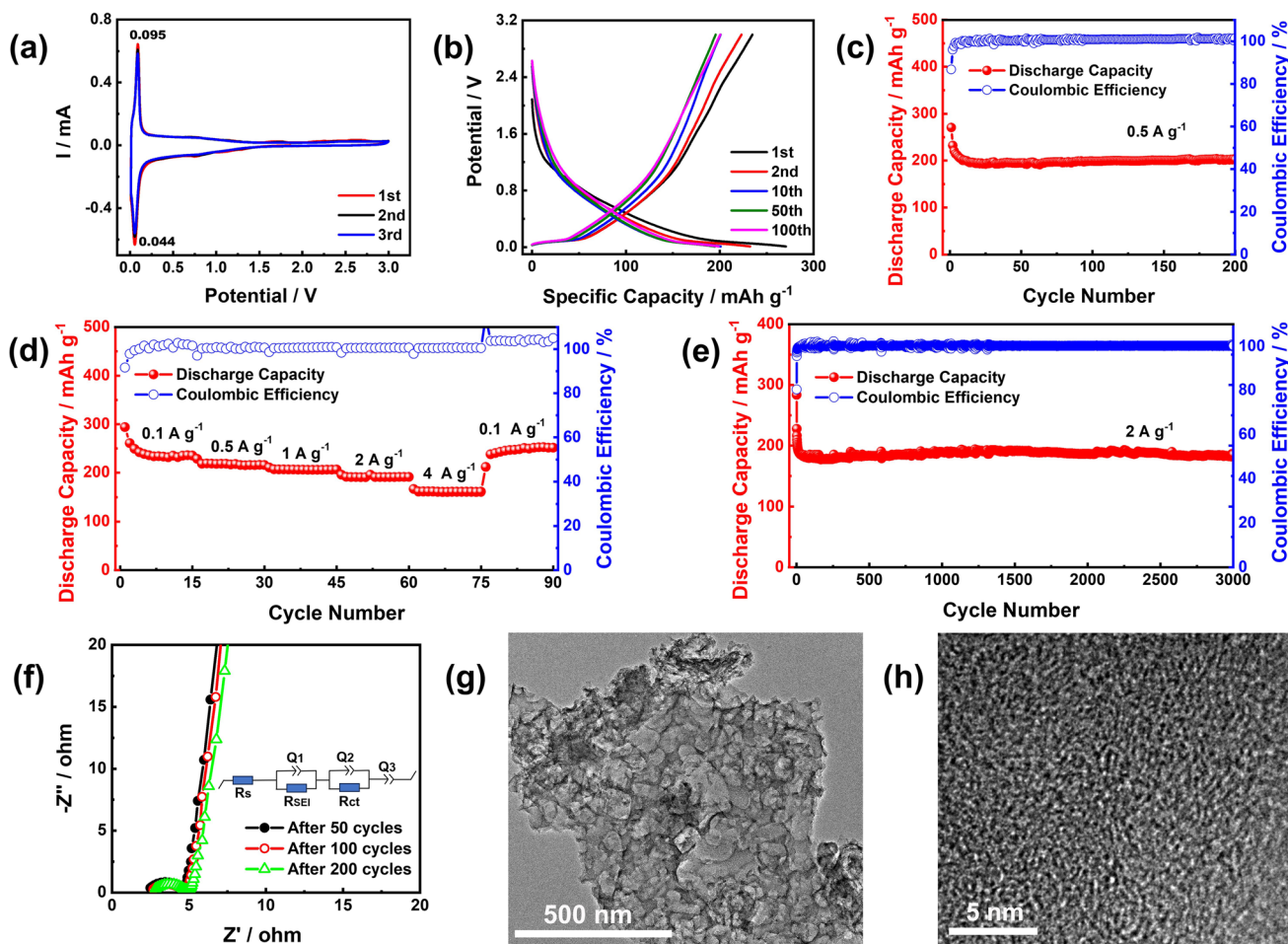
Fig. 3 Electrochemical behaviours and microstructure change of the HS X-C electrodes in Na-ion half cells: **a** CV curves in the first three cycles at 0.2 mV s^{-1}, **b** charge/discharge profiles in different cycles at 0.5 A g^{-1}, **c** cycle performance at 0.5 A g^{-1}, **d** rate capability at 0.1, 0.5, 1, 2 and 4 A g^{-1}, **e** long cycle stability at 2 A g^{-1}, **f** EIS after different cycles and (**g**), **h** TEM images after 1000 cycles

shows the charge–discharge profiles of different cycles at 0.5 A g^{-1}. The discharge profiles could be roughly divided into three characteristic regions. In this region of higher than about 1.15 V, the discharge profile was steep, corresponding to the process of Na$^+$ deposition in the defect area of the material. In the region of less than 0.07 V, the discharge profile was flat, corresponding to the insertion of Na$^+$ into the "pseudo-graphite" layer [33–35]. The intermediate region at 1.0–0.07 V corresponded to the process of Na$^+$ insertion into disordered carbon [36]. The three regional characteristics in the charge profiles were also obvious. The first discharge and charge capacities were 270.5 and 234 mAh g^{-1}, respectively, with a high first coulombic efficiency of 86.5%. Generally, the anode material with high specific surface area delivered a low first coulombic efficiency because extra electrolyte was consumed for the formation of solid electrolyte interface (SEI) film. However, in this work, in addition to no obvious electrolyte decomposition peaks in the first CV cathodic scan, the clear honeycomb structure of the material

could still be observed even after 100 cycles (Fig. S3 (a-c)), indicative of a thin SEI layer. To confirm that the high first coulombic efficiency resulted from the solvent of the electrolyte, ester solvent (EC:DMC:EMC = 1:1:1 Vol%, 5.0% FEC) was used to replace diglyme and the results are shown in Fig. S3 (d-g). From Fig. S3 (d, e), significant differences were observed on the surface of the electrode, where the honeycomb structure of the HS X-C could not be observed due to the covering of a thick SEI film. From Fig. S3 (c, f), in the first CV curve, the electrode cycled in the electrolyte using diglyme as solvent had only negligible reduction peak at 0.74 V, while that cycled in the electrolyte with ester as solvent presented three strong reduction peaks at 0.35, 0.78 and 1.0 V. Moreover, the first coulombic efficiency sharply decreased to 28% (Fig. S3 (g)). Therefore, it could be concluded that diglyme was less prone to reductive decomposition on the surface of the HS X-C. Figure 3c shows the cycle performance of the HS X-C at 0.5 A g^{-1}. In the 200 cycles, although the capacity decreased slowly in the first 8 cycles,

it had maintained at about 202 mAh g^{-1} in the subsequent cycles. When cycling at different current densities from 0.1, 0.5, 1, 2 and 4 A g^{-1}, the stable capacities were 235, 216, 206, 191 and 161 mAh g^{-1}, respectively (Fig. 3d), indicating that the anode possessed superior rate capability. From Fig. 3e, the anode also had long cycle stability at a high current density. After 3000 cycles at 2 A g^{-1}, a discharge capacity of 185 mAh g^{-1} was kept, with capacity retention of 96.9% against the stable capacity of 191 mAh g^{-1}. According to Tab. S1, compared with previously reported biochar anodes for Na-ion batteries, the HS X-C overall exhibited higher specific capacity, better rate capability and more excellent cycle stability.

To understand the reasons for the improvement of electrochemical performance of the HS X-C, in addition to investigating the impedance and structural changes of the electrodes during cycling, the structural influence of the synthesized carbon was also compared. Figure 3f shows the variation of electrochemical impedance with cycle number. All EIS consisted of two semicircles in the medium and high frequency area and a slope line in the low frequency area. In the equivalent circuit diagram, Rs represented the solution resistance, R$_{SEI}$ denoted the resistance associated with the migration of Na-ion through the solid electrolyte interface and Rct was the charge transfer resistance during the electrochemical reaction [37]. The fitting results was shown in Table S2. The Rs and R$_{SEI}$ values after 200 cycles showed only a negligible increase when compared with that after 50 cycles, indicative of high structural stability of the electrode. In addition, the Rct values decreased with the cycle, indicating that the charge transfer speed and the electrochemical reaction rate increased. From the TEM images of the cycled HS X-C electrode in Fig. 3g, h, the honeycomb structure of the material was well maintained after 1000 cycles, indicating that such a structure could indeed accommodate well to the tension generated by volume changes. Fig. S4 shows the cycle performance of the X-C at 2 A g^{-1}, the discharge capacity of which had continuously been declining. After 450 cycles, the discharge capacity decreased to 106 mAh g^{-1}, with a low-capacity retention of 44.7% compared with the second discharge capacity. Evidently, introducing NaCl template during the synthesis of material significantly improved the cyclic stability of carbon from Xanthium sibiricum fruits. The excellent electrochemical performance of the HS X-C should be attributed to its unique microstructure, which not only reduced the transmission path of electrons and ions, but also facilitated the release of tension.

To study the kinetics of the electrode process, CV curves were recorded at different scan rates from 0.2 to 1.4 mV s^{-1}. As shown in Fig. 4a, as scan rate increased, all peaks increased in intensity but there was little change in peak potentials, indicating that the electrochemical reaction was highly reversible. The control step of the electrode process was determined by $I_p = a\nu^b$, where b = 0.5 and 1 represent diffusion control and surface adsorption/reaction control, respectively [38]. Figure 4b presents the relation curve of $\log I_p$ – $\log\nu$ of redox peaks, where b$_R$ and b$_O$ were 0.85 and 0.75, respectively, indicating that the reaction rate was jointly controlled by diffusion and capacitance. The capacitive contribution was further calculated by $I = k_1\nu + k_2\nu^{1/2}$, where $k_1\nu$ and $k_2\nu^{1/2}$ represent the contribution of the surface-driven pseudocapacitive process and the contribution of the diffusion-controlled reaction, respectively [39]. Figure 4c shows the variation of the capacitance contribution with the scanning rate. As the scanning rate increased from 0.2 to 1.4 mV s^{-1}, the capacitance contribution increased from 73 to 86%. Figure 4d shows the capacitance contribution corresponding to different potentials at 0.8 mV s^{-1}. The capacitance contribution between 0.6 and 3 V was significantly greater than that between 0 and 0.2 V, indicating that the electrode process was more controlled by diffusion during Na$^+$ insertion/extraction into/out the pseudo-graphite layer. The diffusion coefficient (D) of Na$^+$ was measured using the GITT technique. The recorded GITT curves was shown in Fig. 4e. D was calculated on the formula as follows:

$$D = 4/\pi\tau \left(\frac{m_B V_M}{M_B S} \right)^2 \left(\frac{\Delta E_S}{\Delta E_\tau} \right)^2$$

where τ is the duration of the pulse current, and m_B is the weight of active material, S is the total area of the electrode, ΔE_s is the voltage change during rest, ΔE_τ is the voltage change during pulse, V_M is the molar volume of the active material and M_B is the molar mass of the active material [40]. In this work, each pulse was composed of 10 min of titration with a current density of 20 mA g^{-1} and 30 min of rest. To reflect the speed of ion diffusion more accurately, the actual surface area of the active material was used to replace the apparent area of the electrode. The relative value of M_B/V_M was calculated based on the following formulation:

$$\rho = \frac{1}{V_{pore} + \frac{1}{\rho_{carbon}}}$$

where ρ (g cm^{-3}) is the density of materials, V_{pore} (cm^3 g^{-1}) is the total pore volume analyzed from the N$_2$ adsorption/desorption isotherm, and ρ_{carbon} is the true density of carbon (2 g cm^{-3}). The calculated Na$^+$ diffusion coefficients for discharge and charge are also shown in Fig. 4e. The D values were between $3.8 \times 10^{-15} \sim 8.2 \times 10^{-17}$ cm^2 s^{-1} during discharging, while the D values were between $5.0 \times 10^{-15} \sim 1.3 \times 10^{-17}$ cm^2 s^{-1} during charging. During discharging, the ion diffusion rate presented a rapid increase between 1.2 and 0.6 V and then gradually decreased until the cutoff voltage, indicating that the micropores were more accessible than the interlayer space in the hard carbon. The
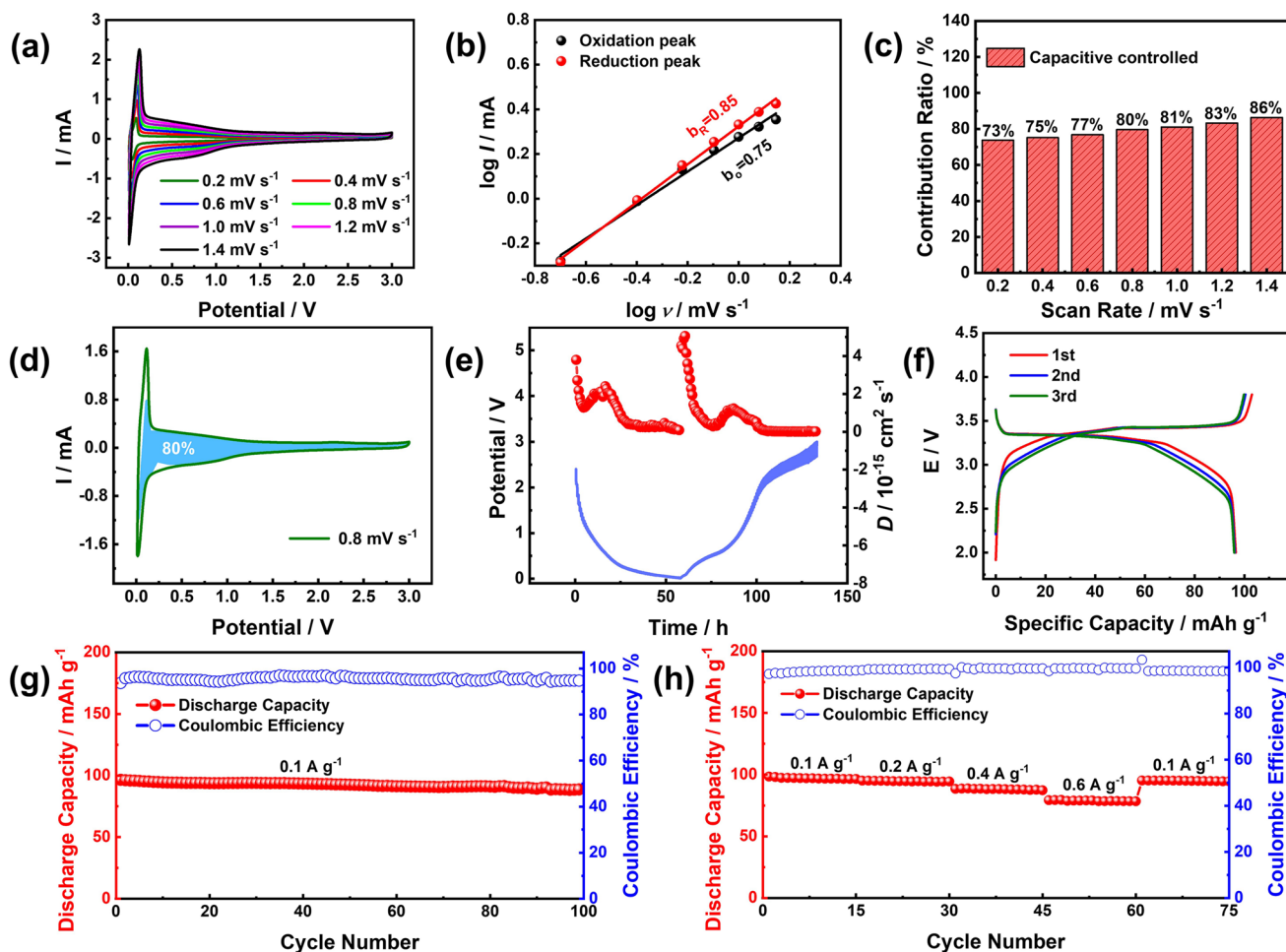
Fig. 4 Dynamics of the HS X-C anodes in Na-ion half cells: **a** CV curves at various scan rates from 0.2 to 1.4 mV s^{-1}, **b** fitting curves of log$I$—log v, **c** capacitance contribution at various scan rates, **d** capacitance contribution of different potential at 0.8 mV s^{-1} and (**e**) GITT curves. Electrochemical performance of HS X-C‖NVP/rGO Na-ion full cell: **f** charge/discharge profiles, **g** cycle performance at 0.1 A g^{-1}(cathode) and (**h**) rate performance at 0.1, 0.2, 0.4 and 0.6 A g.$^{-1}$(cathode)

rapid decline of ion diffusion rate in the plateau region was because Na$^+$ had to overcome a charge repulsion from the Na$^+$ bound in micropores to insert interlayer space [29]. During charging, the detachment of Na$^+$ from micropores was relatively easy, where a sudden increase in ion diffusion rate was also observed.

Full cells were assembled to further evaluate the feasibility of the HS X-C anode, in which the cathode used was NVP/rGO previously reported by our group [27]. Herein, the mentioned current density and specific capacity were calculated on the weight of NVP/rGO. Figure 4f and g show the charge/discharge profiles and cycle performance at 0.1 A g^{-1}(cathode). The charge/discharge profiles displayed a long voltage platform, low polarization and high operating potential. The charge potential plateau reached 3.4 V, ensuring high energy density of full cells. As shown in Fig. 4g, the full cell had good cycle stability. Based on the total weight of the anode and the cathode as well as an average operating

voltage of 3.3 V, it could be calculated that the full cell delivered a high energy density of about 180 Wh kg^{-1}(total). The rate performance is shown in Fig. 4h. When cycling at different current densities from 0.1, 0.2, 0.4, 0.6 and 0.1 A g^{-1}, the stable capacities were 97, 95, 88, 79 and 95 mAh g^{-1}, respectively. These results indicated that the HS X-C was a potential anode for high-performance sodium-ion batteries.

Conclusions

A novel three-dimensional honeycomb-like N, O-doped biochar was successfully synthesized from Xanthium sibiricum by simple milling and pyrolysis with the help of NaCl template. Thanks to unique structure, high specific surface area and abundant defects, the HS X-C exhibited high capacity, excellent rate capability and long cycle stability. The high first coulombic efficiency was because diglyme was less

prone to reductive decomposition on the surface of the HS X-C. The Na-ion full cells paired with the NVP/rGO cathode showed a high average operating voltage of 3.3 V and a high energy density of 180 Wh $kg^{-1}_{(total)}$. The dynamics of the HS X-C anode was jointly controlled by diffusion and pseudocapacitance. This work not only significantly improved the sodium storage performance of biochar from Xanthium sibiricum fruits, but also demonstrated the importance of the synthesis methods of biochar, providing a new perspective for fully utilizing biochar.

Supplementary Information The online version contains supplementary material available at https://doi.org/10.1007/s11581-023-05235-0.

Author contribution Writing-original draft, investigation, material preparation and data analysis: Wei Zhang; supervision, writing—review and editing, funding acquisition and conceptualization: Mingqi Li; data analysis and formal analysis: Yiwen Chen; formal analysis and electrochemical analysis: Zhanwei Zhang.

Data availability All data generated and analyzed during this study are included in this published article and its supplementary information files.

Declarations

Competing interests The authors declare no competing interests.

References

1. Wei Q, Chang X, Wang J, Huang T, Huang X, Yu J, Zheng H, Chen JH, Peng DL (2022) An ultrahigh-power mesocarbon microbeads|Na$^+$-Diglyme|Na$_3$V$_2$(PO$_4$)$_3$ sodium-ion battery. Adv Mater 34(6):2108304
2. Li C, Cao K, Fan Y, Li Q, Zhang Y, Guo Z (2023) Kinetically well-matched porous framework dual carbon electrodes for high-performance sodium-ion hybrid capacitors. J Colloid Interface Sci 652:1356–1366
3. Kim D, Li OL, Kang J (2021) Maximizing the rate capability of carbon-based anode materials for sodium-ion batteries. J Power Sources 481:228973
4. Jiang Y, Wang Y, Ni J, Li L (2021) Molybdenum-based materials for sodium-ion batteries. InfoMat 3(4):339–352
5. Dai S, Wang L, Shen Y, Wang M (2020) Bismuth selenide nanocrystalline array electrodes for high-performance sodium-ion batteries. Appl Mater Today 18:100455
6. Cao K, Zheng R, Wang S, Shu J, Liu X, Liu H, Huang KJ, Jing QS, Jiao L (2020) Boosting coulombic efficiency of conversion-reaction anodes for potassium-ion batteries via confinement effect. Adv Funct Mater 30(52):2007712
7. Pan M, Lu S, Li Y, Li C, Cao K, Fan Y (2023) Copper hydroxyphosphate Cu$_2$(OH)PO$_4$ as conversion-type anode material for lithium-ion batteries. Ionics 29(6):2209–2215
8. Liu H, He Y, Cao K, Wang S, Jiang Y, Liu X, Huang KJ, Jing QS, Jiao L (2021) Stimulating the reversibility of Sb$_2$S$_3$ anode for high-performance potassium-ion batteries. Small 17(10):2008133
9. Cheng X, Shao R, Li D, Yang H, Wu Y, Wang B, Sun C, Jiang Y, Zhang Q, Yu Y (2021) A self-healing volume variation three-dimensional continuous bulk porous bismuth for ultrafast sodium storage. Adv Funct Mater 31(22):2011264
10. Zhang H, Hasa I, Passerini S (2018) Beyond insertion for Na-Ion batteries: nanostructured alloying and conversion anode materials. Adv Energy Mater 8(17):1702582
11. Peng M, Shin K, Jiang L, Jin Y, Zeng K, Zhou X, Tang Y (2022) Alloy-type anodes for high-performance rechargeable batteries. Angew Chem Int Ed 61(33):e202206770
12. Jiang M, Sun N, Ali Soomro R, Xu B (2021) The recent progress of pitch-based carbon anodes in sodium-ion batteries. J Energy Chem 55:34–47
13. Zhao W, Hu X, Ci S, Chen J, Wang G, Xu Q, Wen Z (2019) N-doped carbon nanofibers with interweaved nanochannels for high-performance sodium-ion storage. Small 15(46):1904054
14. Li C, Sun Y, Wu Q, Liang X, Chen C, Xiang H (2020) A novel design strategy of a practical carbon anode material from a single lignin-based surfactant source for sodium-ion batteries. Chem Commun 56(45):6078–6081
15. Bu L, Kuai X, Zhu W, Huang X, Tian K, Lu H, Zhao J, Gao L (2020) Nitrogen-doped double-shell hollow carbon spheres for fast and stable sodium ion storage. Electrochim Acta 356:136804
16. He L, Sun Y, Wang C, Guo H, Guo Y, Li C, Zhou Y (2020) High performance sulphur-doped pitch-based carbon materials as anode materials for sodium-ion batteries. New Carbon Mater 35(4):420–427
17. Sun Y, Shi XL, Yang YL, Suo G, Zhang L, Lu S, Chen ZG (2022) Biomass-derived carbon for high-performance batteries: from structure to properties. Adv Funct Mater 32(24):2201584
18. Song P, Wei S, Di J, Du J, Xu W, Liu D, Wang C, Qiao S, Cao Y, Cui Q, Zhang P, Ma L, Cui J, Wang Y, Xiong Y (2023) Biomass-derived hard carbon microtubes with tunable apertures for high-performance sodium-ion batteries. Nano Res 16:4874–4879
19. Aristote NT, Song Z, Deng W, Hou H, Zou G, Ji X (2023) Effect of double and triple-doping of sulfur, nitrogen and phosphorus on the initial coulombic efficiency and rate performance of the biomass derived hard carbon as anode for sodium-ion batteries. J Power Sources 558:232517
20. Chen Y, Li F, Guo Z, Song Z, Lin Y, Lin W, Zheng L, Huang Z, Hong Z, Titirici M (2023) Sustainable and scalable fabrication of high-performance hard carbon anode for Na-ion battery. J Power Sources 557:232534
21. Kim M, Fernando JFS, Li Z, Alowasheeir A, Ashok A, Xin R, Martin D, Kumar Nanjundan A, Golberg DV, Yamauchi Y, Amiralian N, Li J (2022) Ultra-stable sodium ion storage of biomass porous carbon derived from sugarcane. Chem Eng J 445:136344
22. Hernández-Rentero C, Marangon V, Olivares-Marín M, Gómez-Serrano V, Caballero Á, Morales J, Hassoun J (2020) Alternative lithium-ion battery using biomass-derived carbons as environmentally sustainable anode. J Colloid Interface Sci 573:396–408
23. Senthil C, Park JW, Shaji N, Sim GS, Lee CW (2022) Biomass seaweed-derived nitrogen self-doped porous carbon anodes for sodium-ion batteries: insights into the structure and electrochemical activity. J Energy Chem 64:286–295
24. Kumar DR, Kanagaraj I, Dhakal G, Prakash AS, Shim J (2021) Palmyra Palm tree biomass-derived carbon low-voltage plateau region capacity on Na-ion battery and its full cell performance. J Environ Chem Eng 9(4):105698
25. Li Y, Hu Y, Titirici M, Chen L, Huang X (2016) Hard carbon microtubes made from renewable cotton as high-performance

anode material for sodium-ion batteries. Adv Energy Mater 6(18):1600659

26. Shi G, Han Z, Hu L, Wang B, Huang F (2022) N/O Co-doped hard carbon derived from cocklebur fruit for sodium-ion storage. ChemElectroChem 9(8):e202200138

27. Cai S, Yan F, Zhao Y, Li M, Chen Y, He X, Wang C (2022) Hierarchical micro-composite assembled from Bi spheres and expanded graphite flakes as anodes for sodium-ion half/full cells with excellent comprehensive electrochemical performance. Chem Eng J 430:132938

28. Zheng T, Zhong X, Li M, Yan F, Cai S, Zhang W, Liu L, Wang D (2021) Fabrication of Bi nanospheres assembled microspheres with petal structure ‖ B, N-co-doped C nanosheets hybrid sodium-ion capacitors with ultrahigh power density, high energy density and long cycle life. J Power Sources 515:230638

29. Groen JC, Peffer LAA, Pérez-Ramírez J (2003) Pore size determination in modified micro and mesoporous materials. Pitfalls and limitations in gas adsorption data analysis. Microporous Mesoporous Mat 60(1–3):1–17

30. Wang X, Du J, Zhang Q, Gu L, Cao L, Liang H (2020) In situ synthesis of sustainable highly efficient single iron atoms anchored on nitrogen doped carbon derived from renewable biomass. Carbon 157:614–621

31. Muruganantham R, Wang F, Liu W (2022) A green route N, S-doped hard carbon derived from fruit-peel biomass waste as an anode material for rechargeable sodium-ion storage applications. Electrochim Acta 424:140573

32. Wang H, Chen J, Wang P, Liang C, Yu K (2022) Preparation and mechanism of biomass-derived graphene-like Li^+/Na^+ battery anodes controlled by N/O functional groups and interlayer spacing. J Alloys Compd 918:165785

33. Yan L, Wang J, Ren Q, Fan L, Liu B, Zhang L, He L, Mei X, Shi Z (2022) In-situ graphene-coated carbon microsphere as high initial coulombic efficiency anode for superior Na/K-ion full cell. Chem Eng J 432:133257

34. Bommier C, Surta TW, Dolgos M, Ji X (2015) New mechanistic insights on Na-ion storage in nongraphitizable carbon. Nano Lett 15(9):5888–5892

35. Ren Q, Wang J, Yan L, Lv W, Zhang F, Zhang L, Liu B, Shi Z (2021) Manipulating free-standing, flexible and scalable microfiber carbon papers unlocking ultra-high initial Coulombic efficiency and storage sodium behavior. Chem Eng J 425:131656

36. Anji Reddy M, Helen M, Groß A, Fichtner M, Euchner H (2018) Insight into sodium insertion and the storage mechanism in hard carbon. ACS Energy Lett 3(12):2851–2857

37. Ou J, Wang J, Zhao G, Zou L, Lei Y (2020) Buckwheat derived nitrogen-rich porous carbon material with a high-performance Na-storage. J Porous Mat 27(4):1139–1147

38. Li D, Zhang Y, Sun Q, Zhang S, Wang Z, Liang Z, Si P, Ci L (2019) Hierarchically porous carbon supported Sn_4P_3 as a superior anode material for potassium-ion batteries. Energy Storage Mater 23:367–374

39. Ou H, Huang J, Zhou Y, Zhu J, Fang G, Cao X, Li J, Liang S (2022) Surface-dominated ultra-stable sodium and potassium storage enabled by N/P/O tri-doped porous carbon. Chem Eng J 450:138444

40. Tao L, Yang Y, Wang H, Zheng Y, Hao H, Song W, Shi J, Huang M, Mitlin D (2020) Sulfur-nitrogen rich carbon as stable high capacity potassium ion battery anode: Performance and storage mechanisms. Energy Storage Mater 27:212–225